

## SIMULATIONS OF WIDE-FIELD WEAK LENSING SURVEYS I: BASIC STATISTICS AND NON-GAUSSIAN EFFECTS

MASANORI SATO<sup>1</sup>, TAKASHI HAMANA<sup>2</sup>, RYUICHI TAKAHASHI<sup>1</sup>, MASAHIRO TAKADA<sup>3</sup>, NAOKI YOSHIDA<sup>3</sup>,  
TAKAHIKO MATSUBARA<sup>1</sup>, NAOSHI SUGIYAMA<sup>1,3</sup>

<sup>1</sup> Department of Physics, Nagoya University, Nagoya 464-8602, Japan

<sup>2</sup> National Astronomical Observatory of Japan, Tokyo 181-8588, Japan and

<sup>3</sup> Institute for the Physics and Mathematics of the Universe, University of Tokyo, Chiba 277-8582, Japan

*Draft version October 29, 2018*

### ABSTRACT

We study the lensing convergence power spectrum and its covariance for a standard  $\Lambda$ CDM cosmology. We run 400 cosmological  $N$ -body simulations and use the outputs to perform a total of 1000 independent ray-tracing simulations. We compare the simulation results with analytic model predictions. The semi-analytic model based on Smith et al. (2003) fitting formula underestimates the convergence power by  $\sim 30\%$  at arc-minute angular scales. For the convergence power spectrum covariance, the halo model reproduces the simulation results remarkably well over a wide range of angular scales and source redshifts. The dominant contribution at small angular scales comes from the sample variance due to the number fluctuations of halos in a finite survey volume. The signal-to-noise ratio for the convergence power spectrum is degraded by the non-Gaussian covariances by up to a factor 5 for a weak lensing survey to  $z_s \sim 1$ . The probability distribution of the convergence power spectrum estimators, among the realizations, is well approximated by a  $\chi^2$ -distribution with broadened variance given by the non-Gaussian covariance, but has a larger positive tail. The skewness and kurtosis have non-negligible values especially for a shallow survey. We argue that a prior knowledge on the full distribution may be needed to obtain an unbiased estimate on the ensemble averaged band power at each angular scale from a finite volume survey.

*Subject headings:* gravitational lensing – large-scale structure of the Universe – cosmology: theory – methods: numerical

### 1. INTRODUCTION

Weak gravitational lensing provides a unique probe of the mass distribution in the Universe. By detecting the so-called “cosmic shear”, one can directly measure the power spectrum of mass fluctuations on cosmological scales of tens or even hundreds of mega-parsecs. The significant detections of cosmic shear signals has been reported by various groups, (e.g. Bacon et al. 2000; Kaiser et al. 2000; Van Waerbeke et al. 2000; Wittman et al. 2000; Hamana et al. 2003), and its ability to constrain cosmological parameters has been shown (e.g. Jarvis et al. 2006; Semboloni et al. 2006; Fu et al. 2008).

Weak lensing can also be a powerful probe of the nature of dark energy. The growth rate of mass fluctuations can be measured by “lensing tomography” (e.g. Hu 1999; Huterer 2002; Takada & Jain 2004) which in turn provides tight constraints on the dark energy equation of state. A number of wide-field surveys are planned for this purpose, such as Subaru Weak Lens Survey (Miyazaki et al. 2006), the Panoramic Survey Telescope & Rapid Response System (Pan-STARRS<sup>1</sup>), the Dark Energy Survey (DES<sup>2</sup>), the Large Synoptic Survey Telescope (LSST<sup>3</sup>), and the Joint Dark Energy Mission (JDEM<sup>4</sup>).

However, to attain the full potential of future surveys, it is of great importance to employ adequate statistical measures of weak lensing for estimating cosmological parameters, properly taking into account correlations of the observables between different angular scales and redshifts, i.e. the covariances. Since most useful cosmological information in weak lensing is inherent in small angular scales that are affected by nonlinear clustering regime, the covariance is by nature non-Gaussian. Ichiki et al. (2009) argued that the use of an inaccurate covariance matrix may result in a systematically biased parameter estimate. However, a modeling of the covariance matrix requires an accurate modeling of nonlinear structure formation, which is not so easy.

There are several approaches to modelling the covariance matrix for a given set of cosmological and survey parameters. The most accurate way to obtain predictions for weak-lensing surveys is to perform ray-tracing simulations through large-volume, high-resolution  $N$ -body simulations of cosmic structure formation (Jain et al. 2000; Hamana & Mellier 2001; Vale & White 2003; White & Vale 2004; Fosalba et al. 2008; Teyssier et al. 2009; Hilbert et al. 2009). Over a range of angular scales of interest, the non-Gaussian effects can be significant in weak lensing measurements (White & Hu 2000; Semboloni et al. 2007; Eifler et al. 2009). However, rather expensive calculations are needed to create many independent realizations in this method. A less expensive way would be to use semi-analytic models that are based on, for instance, the so-called “halo model approach” (Cooray & Hu 2001; Takada & Jain

Electronic address: masanori@phys.nagoya-u.ac.jp

<sup>1</sup> <http://pan-starrs.ifa.hawaii.edu/public/>

<sup>2</sup> <http://www.darkenergysurvey.org/>

<sup>3</sup> <http://www.lsst.org/>

<sup>4</sup> <http://jdem.gsfc.nasa.gov/>

2009).

The purpose of this paper is to study the convergence power spectrum and its covariance using ray-tracing simulations for a concordance  $\Lambda$ CDM cosmology. In order to obtain an accurate covariance matrix, we perform 1000 independent ray-tracing simulations. We compare our simulation results with the halo model predictions for the covariance matrix. We also study the cumulative signal-to-noise ratio for measuring the convergence power spectrum taking into account the non-Gaussian errors. Recently, Lee & Pen (2008) studied the angular power spectrum of the SDSS galaxy distribution and showed that the signal-to-noise ratio integrated over a range of multipoles is two orders of magnitude smaller than the case of Gaussian fluctuations. Motivated by their finding, we examine how the cumulative signal-to-noise ratio for the lensing power spectrum measurement is degraded by non-Gaussian errors using our large number of simulation realizations. Furthermore, we will study how the convergence power spectrum estimates are distributed in different realizations: we will study the probability distribution of convergence power spectrum and then compute the higher-order moments, skewness and kurtosis.

The structure of this paper is as follows. In Section 2 we describe the details of  $N$ -body simulations and ray-tracing simulations. In Section 3, after defining the lensing power spectrum, we show the simulation results for power spectrum estimation and then compare the results with the analytical prediction. In Section 4 we study the power spectrum covariance using the simulations and the halo model, and also estimate the expected signal-to-noise ratio for the power spectrum measurement taking into account the non-Gaussian errors. In Section 5 we study the probability distribution of power spectrum estimators in our simulations. Section 6 is devoted to conclusion and discussion.

## 2. NUMERICAL METHODS

### 2.1. The Cosmological $N$ -body Simulations

We use the parallel Tree-Particle Mesh code *Gadget-2* (Springel 2005) in its full Tree-PM mode. We employ  $256^3$  particles for each of two different simulation volumes, 240 and  $480h^{-1}$ Mpc on a side, which are used for ray-tracing simulations for redshift ranges of  $z = [0, 1]$  and  $[1, 3]$ , respectively (see Fig. 1). The smaller volume simulation for lower redshifts is used in order to have higher mass and spatial resolutions because nonlinear clustering is more evolving at lower redshifts. We generate the initial conditions following the standard Zel'dovich approximation. In this step we employed the linear matter transfer function computed from *CAMB* (Lewis et al. 2000). The initial redshift is set to  $z_{\text{init}} = 40$  and 50 for the large- and small-box simulations, respectively. We perform 200 realizations for each sets and hence have a total of 400 realizations.

We adopt the concordance  $\Lambda$ CDM model with matter density  $\Omega_m = 0.238$ , baryon density  $\Omega_b = 0.042$ , dark energy density  $\Omega_\Lambda = 0.762$  with equation of state parameter  $w = -1$ , spectral index  $n_s = 0.958$ , the variance of the density fluctuation in a sphere of radius  $8 h^{-1}$ Mpc  $\sigma_8 = 0.76$ , and Hubble parameter  $h = 0.732$ . These parameters are consistent with the WMAP 3-year results (Spergel et al. 2007).

We have checked that our simulation result for the convergence power spectrum agrees with the result using  $512^3$  particles within 5 % at  $l \lesssim 10^4$ . This is sufficient for our purpose, which is to study the power spectrum and the covariance down to arcminute scales.

### 2.2. Ray-tracing Simulations

Fig. 1 shows the design of our ray-tracing simulations. We place the small- and large-volume simulations to cover a light cone of angular size  $5^\circ \times 5^\circ$ , from redshift  $z = 0$  to  $z \sim 3.5$ , using the tiling technique developed in White & Hu (2000) and Hamana & Mellier (2001).

We use the standard multiple lens plane algorithm in order to simulate the distortion and magnification of background light rays by foreground matter. Let us briefly describe the procedure to trace light rays through  $N$ -body data (Jain et al. 2000). In the standard multiple lens plane algorithm, the distance between observer and source is divided into  $N$  intervals, separated by comoving distance  $\Delta\chi$ . We adopt a fixed interval between lens planes by  $\Delta\chi = 120h^{-1}$ Mpc (for this choice, the simulation box side lengths become multiples of  $120h^{-1}$ Mpc). The projected density contrast of the  $p$ -th plane is given by

$$\Sigma_p(\boldsymbol{\theta}) = \int_{\chi_{p-1}}^{\chi_{p-1} + \Delta\chi} d\chi \delta(\chi\boldsymbol{\theta}, \chi), \quad (1)$$

where  $\delta$  is the three-dimensional density fluctuation field along the line-of-sight,  $\delta \equiv \rho/\bar{\rho} - 1$ , and  $\chi_{p-1}$  denotes the  $\chi$ -position of  $(p-1)$ -th lens plane, and  $\boldsymbol{\theta}$  is the two-dimensional vector denoting the angular position on the sky. The projected density field is computed on  $4096^2$  grids by projecting  $N$ -body particle distribution onto the lens plane based on the triangular-shaped cloud (TSC) assignment scheme (Hockney & Eastwood 1988). An effective two-dimensional gravitational potential of the  $p$ -th plane is related to projected density contrast via the two-dimensional Poisson equation

$$\nabla^2\psi_p = 3 \left( \frac{H_0}{c} \right)^2 \Omega_m \Sigma_p. \quad (2)$$

This equation is solved to compute  $\psi_p$  using the fast Fourier transform method making use of the periodic boundary conditions. Then, the first and second derivatives of  $\psi_p$  are evaluated on each grid point. Next,  $2048^2$  rays are traced backward from the observer point. The initial ray directions are set on  $2048^2$  grids, which correspond to angular grid size of  $5^\circ/2048 \sim 0.15$  arcmin. For each ray, we first computed ray positions on all the lens planes using the lens equation:

$$\boldsymbol{\theta}_n = - \sum_{p=1}^{n-1} \frac{f_K(\chi_n - \chi_p)}{f_K(\chi_n)} \nabla_\perp \psi_p + \boldsymbol{\theta}_1, \quad (3)$$

where  $f_K(\chi)$  is the comoving angular diameter distance given as function of  $\chi$ ;  $f_K(\chi) = \chi$  for a flat universe. The first and second derivatives of  $\psi_p$  on a ray position are linearly interpolated from four nearest grids on which they were pre-computed. The evolution equation of the Jacobian matrix, which describes deformation of an in-

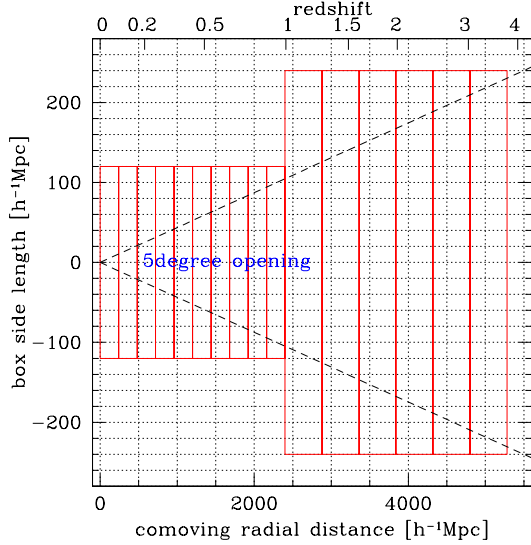


FIG. 1.— The design of our ray-tracing simulations. Dashed lines show the field-of-view spanning  $\pm 2.5$  degree.

finitesimal light ray bundle, is written as

$$\mathbf{A}_n = \mathbf{I} - \sum_{p=1}^{n-1} \frac{f_K(\chi_p) f_K(\chi_n - \chi_p)}{f_K(\chi_n)} \mathbf{U}_p \mathbf{A}_p, \quad (4)$$

where  $\mathbf{I}$  is the identity matrix, and  $\mathbf{U}_p$  is the shear tensor on the  $p$ -th lens plane defined by

$$\mathbf{U}_{ij} \equiv \frac{\partial^2 \psi_p}{\partial x_i \partial x_j}, \quad (5)$$

where  $x_i \equiv \chi \theta_i$  and so on. The Jacobian matrix is usually decomposed as

$$\mathbf{A} = \begin{pmatrix} 1 - \kappa - \gamma_1 & -\gamma_2 - w \\ -\gamma_2 + w & 1 - \kappa + \gamma_1 \end{pmatrix}, \quad (6)$$

where  $\kappa$  is convergence,  $|\gamma| = (\gamma_1^2 + \gamma_2^2)^{1/2}$  is the magnitude of the shear, and  $w$  is a net beam rotation. Finally, the summation in Eq. (4) yields the Jacobian matrix. The light-ray positions and four components of the Jacobian matrix on desired source planes are stored. Source redshifts we consider in this paper are summarized in Table.1

We perform 1000 ray-tracing realizations of the underlying density field by randomly shifting the simulation boxes assuming periodic boundary conditions. In doing this, each simulation output is shifted in the same way to make several lens planes to maintain the clustering pattern of mass distribution within the simulation box<sup>5</sup>. Importantly, however, in order to have *independent* realizations, we do not use the same simulation output when making each ray-tracing realization. Note that we use only one projection axis to all ray-tracing realizations, unlike many previous works in which three orthogonal directions are used to increase the number of *realizations*.

<sup>5</sup> Note that, for the separation between lens planes  $\Delta\chi = 120h^{-1}\text{Mpc}$ , we make two (four) lens planes from one simulation output for the redshift range  $z = [0, 1]$  ( $z = [1, 3]$ ) because we use simulations of different volumes as described in § 2.1.

TABLE 1  
SOURCE REDSHIFTS EMPLOYED FOR OUR RAY-TRACING SIMULATIONS.

$z_s$	exact values
0.6	0.588542
0.8	0.810822
1.0	0.996884
1.5	1.51902
2.0	1.99765
3.0	3.05725

### 3. POWER SPECTRUM

The mass density power spectrum  $P_\delta(k)$  is defined as

$$\langle \tilde{\delta}(\mathbf{k}) \tilde{\delta}^*(\mathbf{k}') \rangle = (2\pi)^3 \delta_D^3(\mathbf{k} - \mathbf{k}') P_\delta(k). \quad (7)$$

Likewise to Eq. (7), one can define the convergence power spectrum  $P_\kappa(l)$  as

$$\langle \tilde{\kappa}(\mathbf{l}) \tilde{\kappa}^*(\mathbf{l}') \rangle = (2\pi)^2 \delta_D^2(\mathbf{l} - \mathbf{l}') P_\kappa(l). \quad (8)$$

The conversion from the 3-D wave vector  $\mathbf{k}$  to the 2-D angular wave vector  $\mathbf{l}$  is done by the line of sight integration using the Limber approximation (Limber 1954; Kaiser 1998). By using the Limber approximation, the convergence power spectrum is given by (see, e.g. Bartelmann & Schneider 2001; Van Waerbeke & Mellier 2003)

$$P_\kappa(l) = \int_0^{\chi_H} d\chi \frac{W(\chi)^2}{f_K(\chi)^2} P_\delta\left(\frac{l}{f_K(\chi)}; \chi\right), \quad (9)$$

where  $\chi_H$  is the horizon distance, defined as the comoving distance obtained for infinite redshift. The weight function  $W(\chi)$  is now

$$W(\chi) = \frac{3}{2} \frac{H_0^2 \Omega_m}{c^2 a(\chi)} f_K(\chi) \int_\chi^{\chi_H} d\chi' G(\chi') \frac{f_K(\chi' - \chi)}{f_K(\chi')}, \quad (10)$$

where  $G(\chi)$  is the probability distribution of sources in comoving distance. For simplicity, all sources are assumed to be located at the same redshift  $z_s$ , so that

$$G(z) = \delta_D(z - z_s). \quad (11)$$

The binned convergence power spectrum can be estimated from each realization as

$$\hat{P}_\kappa(l) = \frac{1}{N_l} \sum_{\mathbf{l}; |\mathbf{l}| \in l} |\tilde{\kappa}(\mathbf{l})|^2, \quad (12)$$

where the summation runs over modes whose lengths lie in the range  $l - \Delta l/2 \leq |\mathbf{l}_i| \leq l + \Delta l/2$  for the assumed bin width  $\Delta l$ . Throughout this paper we employ the bin width  $\Delta \ln l = 0.3$ . The number of modes around a bin  $l$  is approximately given by

$$N_l \approx A_s \cdot \Omega_s / (2\pi)^2, \quad (13)$$

where  $A_s$  is the area of the two-dimensional shell around the bin  $l$  and can be given as  $A_s \approx 2\pi l \Delta l + \pi(\Delta l)^2$ , and  $\Omega_s$  is the survey area. Taking the average of Eq. (12) over a number of realizations is expected to give the ensemble average expectation  $P_\kappa(l) = \langle \hat{P}_\kappa(l) \rangle$ .

Fig. 2 shows the convergence power spectrum obtained from our ray-tracing simulations for  $z_s = 1.0$ . We

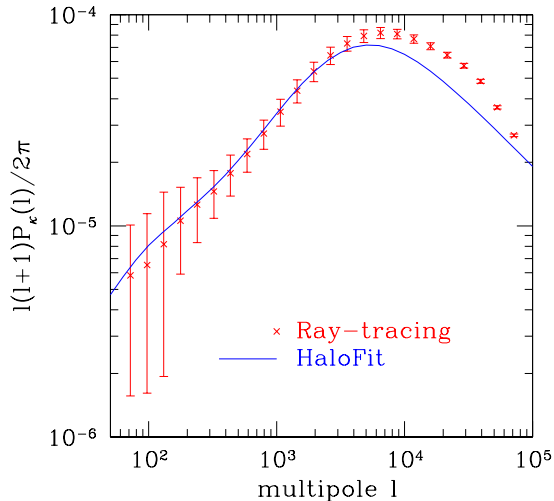


FIG. 2.— Convergence power spectrum for sources at redshift  $z_s = 1.0$ . The result from our 1000 ray-tracing simulations is shown as the cross symbols with error bars ( $\pm 1\sigma$  variance). We also show the semi-analytic prediction computed from Eq. (9) using *HaloFit* to model the 3D mass power spectrum.

compare it with the semi-analytic prediction computed using the Smith et al. (2003) fitting formula (hereafter *HaloFit*) to compute the nonlinear matter power spectrum  $P_\delta(k)$ . The *HaloFit* underpredicts the convergence power at intermediate and small scales,  $l > 3000$ . A similar disagreement is also found in Hilbert et al. (2009) using Millennium Simulation (Springel et al. 2005) which has higher mass and spatial resolutions than ours.

To further explore the cause of this discrepancy, we study the three-dimensional mass power spectra using our  $N$ -body simulations. Fig. 3 compares the power spectra obtained from 200 realizations with the *HaloFit* predictions at  $z = 0$  and 0.92. The arrow shows the Nyquist wavenumber. The *HaloFit* results are approximately 5–10% lower than the results from simulations. Heitmann et al. (2008) also report a similar disagreement. It appears that the discrepancy in the convergence power at high  $l$  is owing to inaccuracy in *HaloFit*.

We also examine the effect of smoothing used in ray-tracing simulations by varying the grid size. Fig. 4 compares the convergence power spectra calculated for two different grid sizes,  $2048^2$  and  $4096^2$  grids, respectively. Clearly, the coarser grid size yields a smaller power at  $l > 3000$ . In the bottom panel, we show that the difference reaches  $\sim 5\%$  at  $l \sim 3000$ . When we compute the projected density field, we would naively expect that a finer grid size provides a higher resolution in the lensing convergence map, if the original  $N$ -body simulation has a sufficient spatial resolution. Further halving the grid size, i.e. changing the grid number to  $8192^2$  from  $4096^2$ , is similarly thought to give a better accuracy up to higher multipoles. We have checked the difference reaches  $\sim 5\%$  at  $l \sim 6000$ . Therefore, we conclude that estimating power spectrum from the projected density fields on  $4096^2$  grids is sufficiently accurate up to  $l \sim 6000$ . In the following section, we focus on the power spectrum information up to  $l \sim 6000$ .

#### 4. COVARIANCE MATRIX

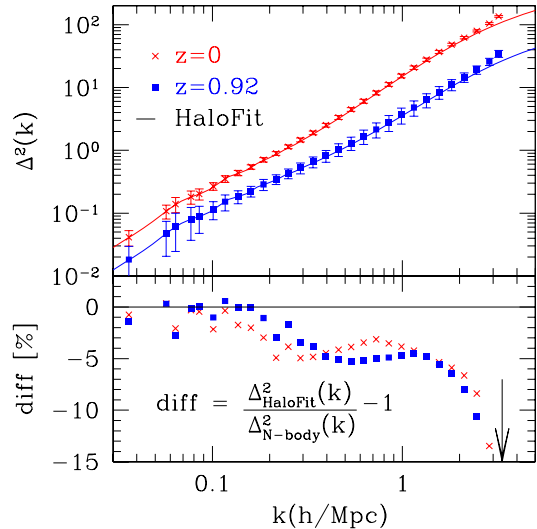


FIG. 3.— *Top panel*: Comparison of the dimensionless 3D mass power spectrum,  $\Delta^2(k) = k^3 P(k)/2\pi^2$ , obtained from 200 realizations to the *HaloFit* prediction at  $z = 0$  and 0.92. *Bottom panel*: The fractional difference is shown in percent. The arrow shows the Nyquist wavenumber.

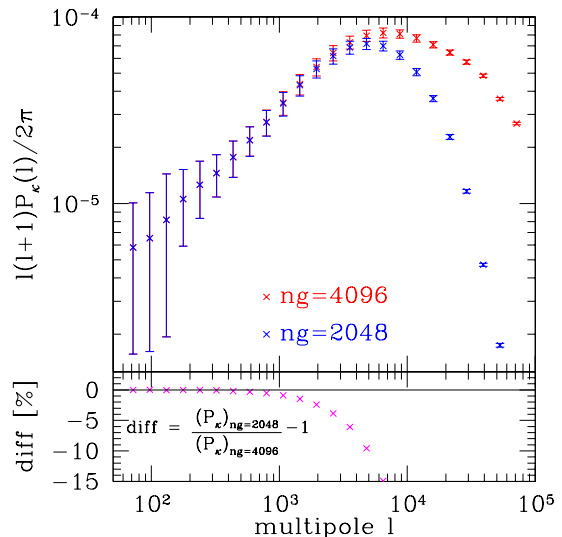


FIG. 4.— The effect of grid size in ray-tracing simulation on the power spectrum estimation. *Top panel*: The two spectra computed from 1000 realizations employing  $2048^2$  and  $4096^2$  grids. *Bottom panel*: The fractional difference is shown in percent.

The covariance matrix of the convergence power spectrum between  $P_\kappa(l)$  and  $P_\kappa(l')$  is formally expressed as a sum of the Gaussian and non-Gaussian contributions (e.g. Scoccimarro et al. 1999; Cooray & Hu 2001):

$$\begin{aligned} \text{Cov}[P_\kappa(l), P_\kappa(l')] &\equiv \left\langle \left( \hat{P}_\kappa(l) - P_\kappa(l) \right) \left( \hat{P}_\kappa(l') - P_\kappa(l') \right) \right\rangle \\ &= \frac{2}{N_l} P_\kappa(l)^2 \delta_{l,l'}^K \\ &+ \frac{1}{\Omega_s} \int_l \frac{d^2 \mathbf{l}}{A_s} \int_{l'} \frac{d^2 \mathbf{l}'}{A_{s'}} T(\mathbf{l}, -\mathbf{l}, \mathbf{l}', -\mathbf{l}'), \end{aligned} \quad (14)$$

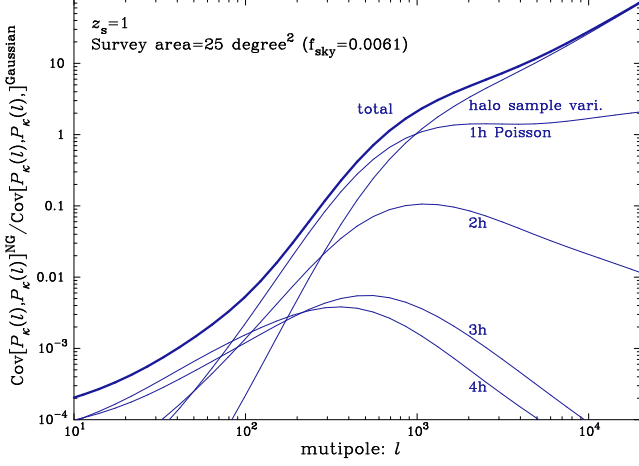


FIG. 5.— The halo model predictions for the ratio of the diagonal non-Gaussian covariance components to the Gaussian errors as a function of multipole, where the Gaussian errors are given by  $\text{Cov}^G = P_\kappa(l)^2 / (f_{\text{sky}} l^2 \Delta \ln l)$ . Note that we assume source redshift  $z_s = 1$ , the survey area  $\Omega_s = 25$  sq. degrees and the multipole bin width  $\Delta \ln l = 0.3$ . In our halo model the non-Gaussian errors are given by the sum of the different halo terms of trispectrum contribution (see Eqs. 14 and 17) and the halo sample variance (see Eq. 18). The thick solid curve shows the total contribution to the non-Gaussian errors, while the thin solid curves show each different term contributions as indicated by each label.

where  $\delta_{l,l'}^K$  is the Kronecker delta function and  $T$  is the lensing trispectrum defined as

$$\langle \tilde{\kappa}(\mathbf{l}_1) \tilde{\kappa}(\mathbf{l}_2) \tilde{\kappa}(\mathbf{l}_3) \tilde{\kappa}(\mathbf{l}_4) \rangle \equiv (2\pi)^2 \delta_D(\mathbf{l}_{1234}) T(\mathbf{l}_1, \mathbf{l}_2, \mathbf{l}_3, \mathbf{l}_4), \quad (15)$$

where we have introduced notation  $\mathbf{l}_{1234} = \mathbf{l}_1 + \mathbf{l}_2 + \mathbf{l}_3 + \mathbf{l}_4$ . In the Limber approximation,  $T$  is a simple projection of the three-dimensional mass trispectrum  $T_\delta$  given by

$$T(\mathbf{l}_1, \mathbf{l}_2, \mathbf{l}_3, \mathbf{l}_4) = \int_0^{\chi_H} d\chi \frac{W(\chi)^4}{f_K(\chi)^6} \times T_\delta \left( \frac{\mathbf{l}_1}{f_K(\chi)}, \frac{\mathbf{l}_2}{f_K(\chi)}, \frac{\mathbf{l}_3}{f_K(\chi)}, \frac{\mathbf{l}_4}{f_K(\chi)}; \chi \right). \quad (16)$$

In Eq. (14), the first term describes the Gaussian error contribution that has vanishing correlations between different multipole bins, whereas the second term describes the non-Gaussian contribution arising from mode coupling due to nonlinear clustering. Both the terms scale with the survey area as  $\propto 1/\Omega_s$ . It should be also noted that the Gaussian term depends on the bin width  $\Delta l$ , whereas the non-Gaussian term does not (because  $\int_l d^2 \mathbf{l} / A_s \approx 1$ ). Thus decreasing  $\Delta l$  increases the Gaussian contribution relative to the non-Gaussian errors.

#### 4.1. Halo Model Approach for the Covariance

To make an analytic estimation of the lensing power covariance using Eq. (14), we need to model the mass trispectrum that can account for the non-linear clustering at small angular scales. In this paper we employ the halo model approach (Seljak 2000; Ma & Fry 2000; Peacock & Smith 2000, also see Cooray & Sheth (2002) for a thorough review). In the halo model, the power spectrum is given by a sum of two terms: the so-called 1-halo term which describes correlation of dark matter particles within each halo, and the 2-halo term which describes correlation of particles in different halos. Likewise, the trispectrum consists of four terms, from one to

four halo terms (Cooray & Hu 2001):

$$T_\delta = T_\delta^{1h} + T_\delta^{2h} + T_\delta^{3h} + T_\delta^{4h}, \quad (17)$$

where we have suppressed the arguments  $(\mathbf{k}_1, \mathbf{k}_2, \mathbf{k}_3, \mathbf{k}_4)$  of  $T_\delta$ . These four terms contribute to the power at each  $l$  differently. The 1-halo term gives dominant contribution in the nonlinear clustering regime.

To complete the halo model approach, we need suitable models for the three ingredients: the halo mass density profile, the mass function of halos, and the biasing of halo distribution, each of which is specified by halo mass  $m$  and redshift  $z$  for a given cosmological model. For these we employ an NFW profile (Navarro et al. 1997), and the fitting formulae for mass function and halo bias derived in Sheth & Tormen (1999). The details of our halo model implementation can be found in Takada & Jain (2003a) (also see Takada & Jain 2003b).

However it turns out there is additional contribution to the non-Gaussian covariance, which becomes significant on small scales as described below. As first pointed out in Hu & Kravtsov (2003), the halo clustering causes additional sampling variance to the covariance due to the statistical fluctuations in the number of halos sampled by a *finite* survey volume (also see Takada & Bridle 2007; Neyrinck et al. 2006; Zhang & Sheth 2007; Reid & Spergel 2009). In simpler words, if massive halos happen to be more (less) in a surveyed region, the measured power spectra would very likely have greater (smaller) amplitudes than expected from the ensemble average.

According to the formulation developed in Appendix in Takada & Bridle (2007) (also see the discussion around Eq. (7) in Zhang & Sheth 2007), the sample variance to which we hereafter refer as the halo sample variance (HSV) is expressed as

$$\begin{aligned} \text{Cov}_{\text{HSV}}[P_\kappa(l), P_\kappa(l')] &= \int_0^{\chi_s} d\chi \left( \frac{d^2 V}{d\chi d\Omega} \right)^2 \\ &\times \left[ \int dM \frac{dn}{dM} b(M) |\tilde{\kappa}_M(l)|^2 \right] \\ &\times \left[ \int dM' \frac{dn}{dM'} b(M') |\tilde{\kappa}_{M'}(l')|^2 \right] \\ &\times \int_0^\infty \frac{k dk}{2\pi} P_\delta^L(k; \chi) \left| \tilde{W}(k\chi\Theta_s) \right|^2, \quad (18) \end{aligned}$$

where  $d^2 V / d\chi d\Omega$  is the comoving volume per unit solid angle and unit radial comoving distance, given as  $d^2 V / d\chi d\Omega = \chi^2$  for a flat universe,  $\chi_s$  is the comoving distance to a source redshift  $z_s$ ,  $dn/dM$  is the halo mass function,  $b(M)$  is the halo bias parameter, and  $\tilde{\kappa}_M(l)$  is the angular Fourier-transform of the convergence field for a halo with mass  $M$  (see Eqs. 28 and 31 in Takada & Jain 2003a, for the definition). The quantity  $P_\delta(k)$  is the linear 3D mass power spectrum, and  $\tilde{W}(x)$  is the Fourier transform of the survey window function; for this we simply employ  $\tilde{W}(k\chi\Theta_s) = 2J_1(k\chi\Theta_s) / (k\chi\Theta_s)$  ( $J_1(x)$  is the first-order Bessel function) assuming  $\Theta_s = \sqrt{\Omega_s / \pi}$  for a given survey area  $\Omega_s$ . Thus we have assumed that the survey area is sufficiently large and the number fluctuations of halos are in the linear regime. Note that this sampling variance contribution does not necessarily scale

with  $1/f_{\text{sky}}$  unlike other covariance terms. The sample variance depends on  $f_{\text{sky}}$  via the shape of linear power spectrum. For a CDM spectrum it becomes smaller with increasing  $\Omega_s$ , and decreases faster than the other covariance terms that have the scaling of  $\Omega_s^{-1}$  or  $f_{\text{sky}}^{-1}$  if  $\Omega_s$  is greater than a few hundreds square degrees, for multipoles of interest ( $l \gtrsim 1000$ ).

More exactly Eq. (18) was derived by replacing the function  $S_{(b)}$  in Eq. (B1) of Takada & Bridle (2007) with  $|\tilde{\kappa}_M(l; z)|^2$ , which is the lensing power spectrum contribution due to a halo with mass  $M$  and at redshift  $z$ . In fact the first term on the r.h.s. of Eq. (B1) corresponds to the 1-halo term of non-Gaussian errors in Eq. (14), while the second term in Eq. (B1) yields Eq. (18). The contribution of Eq. (18) arises for any finite-volume survey because the halo distribution has modulations due to the biased density fluctuations over the survey window. The full derivation of non-Gaussian covariance within the context of the halo model approach is beyond the scope of this paper and will be presented elsewhere.

To obtain a more physical insight, it would be useful to note that the sample variance (18) is roughly expressed as

$$\text{Cov}_{\text{HSV}} \sim \bar{b}^2 \sigma_{\text{rms}}^2(\Theta_s) P_{\kappa}^{1\text{h}}(l) P_{\kappa}^{1\text{h}}(l'), \quad (19)$$

where  $\bar{b}$  is the halo bias averaged over halo masses and redshift interval,  $\sigma_{\text{rms}}(\Theta_s)$  is the rms of angular mass density fluctuations for the survey area, and  $P_{\kappa}^{1\text{h}}(l)$  is the 1-halo term of the convergence power spectrum. Here the combination of  $\bar{b}\sigma_{\text{rms}}(\Theta_s)$  gives the rms fluctuations in the number of halos in the survey area. Thus the sample variance strength is proportional to combined effect of the convergence power spectrum and the number fluctuations of massive halos due to the large-scale mass density fluctuations. The sample variance (18) is vanishing if the halo distribution does not have any clustering, i.e. is completely random (corresponding to the limit  $\bar{b}\sigma_{\text{rms}} \rightarrow 0$ ). Note that, on the other hand, the 1-halo term of the trispectrum accounts for the Poisson contribution to the sample variance arising from the discreteness nature of halo distribution.

Fig. 5 shows the halo model predictions for the diagonal non-Gaussian covariances relative to the Gaussian errors as a function of multipoles. Note that we consider source redshift  $z_s = 1$  as a representative example, but the results are very similar for other source redshifts we consider in this paper. The different halo term contributions to the covariance are more important on small multipoles, while the 1-halo term becomes increasingly significant with increasing multipoles. Importantly the sample variance contribution due to the number fluctuations of massive halos, given by Eq. (18), becomes dominant over other non-Gaussian errors at high multipoles  $l \gtrsim 1000$ , boosting the non-Gaussian error strengths by an order of magnitude up to  $l \sim 10^4$  from the estimate without this new effect. For high multipole limit, the ratio of the diagonal non-Gaussian covariance to the Gaussian errors has an asymptotic scaling as  $\text{Cov}^{\text{NG}}/\text{Cov}^{\text{G}} \sim \bar{b}^2 \sigma_{\text{rms}}^2 P_{\kappa}^{1\text{h}}(l) P_{\kappa}^{1\text{h}}(l) / [2P_{\kappa}^{1\text{h}}(l)^2 / N_l] \sim \bar{b}^2 \sigma_{\text{rms}}^2(\Theta_s) N_l / 2 \propto l^2 \Delta \ln l$ . Hence,  $\text{Cov}^{\text{NG}}/\text{Cov}^{\text{G}} \propto l^2$  for a constant bin width  $\Delta \ln l$  as implied from the results around  $l \sim 10^4$  in Fig. 5, because  $\bar{b}\sigma_{\text{rms}}(\Theta_s)$  is constant for fixed survey area and cosmological model.

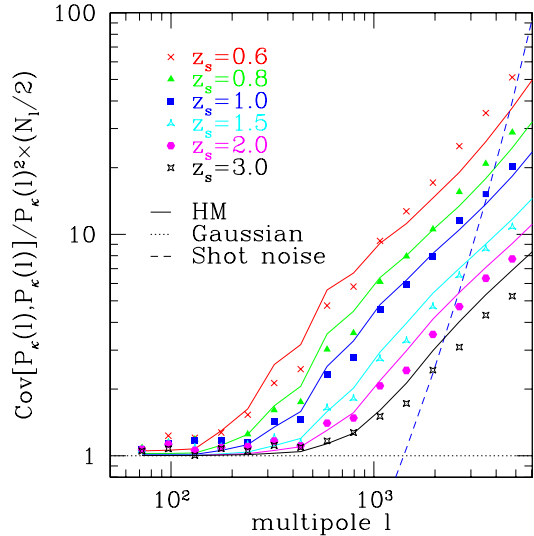


FIG. 6.— The diagonal components of the convergence power spectrum covariance for  $z_s = 0.6, 0.8, 1.0, 1.5, 2.0$  and  $3.0$ , respectively. The results are divided by the expected Gaussian covariance (the first term in Eq. (14)). Therefore, the deviations from unity arise from the non-Gaussian errors. The symbols are the simulation results, while the solid curves are the halo model predictions. The shot noise contribution for source redshift  $z_s = 1.0$  assuming  $\bar{n}_g = 30 \text{ arcmin}^{-2}$  and  $\sigma_\epsilon = 0.22$  for the mean number density and the rms intrinsic ellipticities, respectively.

This contribution has been ignored in previous studies and we will below study the impact on the lensing power spectrum covariance comparing the halo model predictions with the simulation results.

#### 4.2. Diagonal Components of the Covariance Matrix

Fig. 6 shows the diagonal components of the convergence power spectrum covariance as a function of multipole. The values are divided by the expected Gaussian covariances for the power spectrum, which is estimated by inserting the power spectrum measured from the simulations into the first term on the r.h.s. of Eq. (14). Therefore, the deviations from unity arise from the non-Gaussian error contribution. The different symbols are the simulation results for different redshifts. It is clear that the non-Gaussian errors start to be significant at multipoles from a few hundreds, and the non-Gaussian errors are greater for lower source redshifts due to stronger nonlinearities in the large-scale structure.

For comparison, the solid curves show the halo model predictions including the sample variance contribution due to the number fluctuations of halos in the simulation volume as described around Eq. (18). Note that, to obtain the halo model prediction, the survey area is set to  $\Omega_s = 25 \text{ deg}^2$  as assumed for the ray-tracing simulations. Rather unexpectedly the empirical halo model fairly well reproduces the simulation results over a wide range of multipoles and for redshifts we have considered. It should be noted that the agreement cannot be found if the sample variance (18) is not included: the sample variance is dominant over other non-Gaussian covariance terms at multipoles  $l \gtrsim 1000$  (see Fig. 5). The  $l$ -dependence of the ratio at these high multipoles is approximately given as  $\text{Cov}^{\text{NG}}/\text{Cov}^{\text{G}} \propto l^1$  for all source redshifts, shallower than the asymptotic behavior  $\propto l^2$  discussed below Eq. (19) due to the residual contribu-

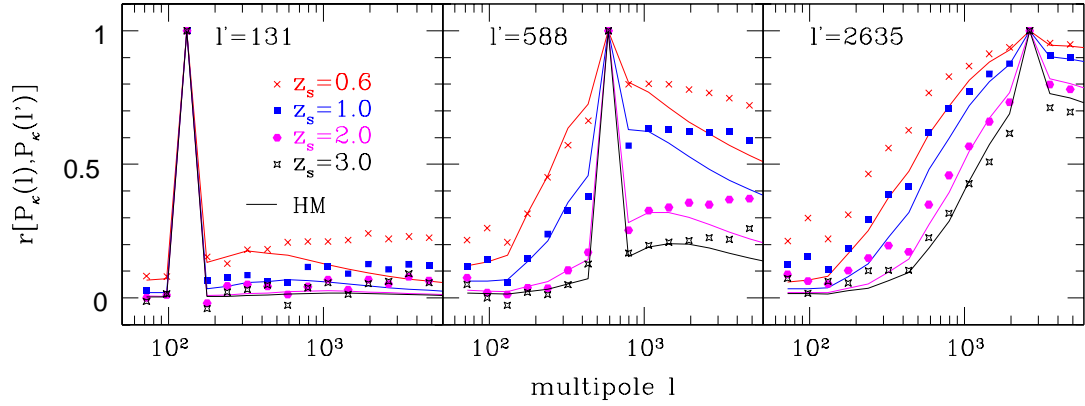


FIG. 7.— The correlation coefficients  $r[P_\kappa(l), P_\kappa(l')]$  as a function of  $l$  for a given  $l'$ , where  $l'$  is chosen to  $l' = 131$  (left panel),  $588$  (middle) and  $l' = 2635$  (right), respectively. The solid curves denote the halo model predictions. Although the simulation and halo model results are in fairly good agreement, the simulations results display slightly greater correlation strengths for high multipoles and at lower redshifts.

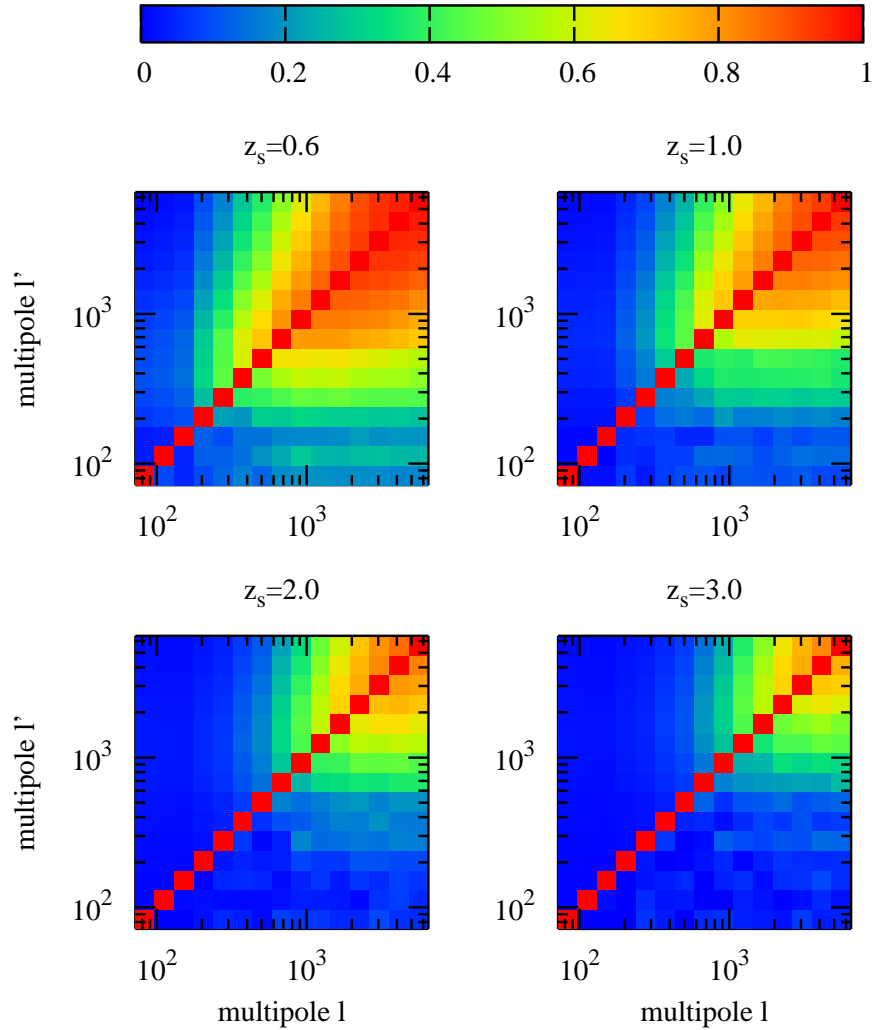


FIG. 8.— Comparison of the covariance correlation matrices predicted by the halo model (upper triangular parts of the matrices) and those obtained from our 1000 ray-tracing simulations (lower triangular parts) for  $z_s = 0.6, 1.0, 2.0$  and  $3.0$ .

tions of other non-Gaussian covariance terms.

In practice, the shot noise contamination due to intrinsic galaxy ellipticities contributes to the diagonal term of the covariance. The dashed line denotes the contribution for source redshift  $z_s = 1.0$  assuming  $\bar{n}_g = 30 \text{ arcmin}^{-2}$  and  $\sigma_\epsilon = 0.22$  for the mean number density and the rms intrinsic ellipticities, respectively, which are typical numbers for a ground-based weak lensing survey such as the planned Subaru weak lensing survey. It is found that the shot noise becomes significant compared to the cosmological non-Gaussian contributions at very high multipoles, thereby making the covariance be closer to Gaussian in the multipole range.

#### 4.3. Off-Diagonal Components of the Covariance Matrix

The correlation coefficients of the convergence power spectrum covariances quantify the relative strengths of the off-diagonal components to the diagonal components. The correlation coefficient is defined as

$$r[P_\kappa(l), P_\kappa(l')] = \frac{\text{Cov}[P_\kappa(l), P_\kappa(l')]}{\sqrt{\text{Cov}[P_\kappa(l), P_\kappa(l)]\text{Cov}[P_\kappa(l'), P_\kappa(l')]}}, \quad (20)$$

Thus the correlation coefficient is defined so as to give unity when  $l = l'$ . For off-diagonal components  $r \rightarrow 1$  implies strong correlation between the two spectra of different multipoles, while  $r \rightarrow 0$  means no correlation.

Fig. 7 shows the correlation coefficients  $r(l, l')$  as a function of  $l$  for a given  $l'$  and at  $z_s = 0.6, 1.0, 2.0$  and  $3.0$ . Note that the results depend on the bin width. The solid curves denote the halo model predictions. The halo model predictions fairly well reproduce the simulation results. A closer look implies a sizable disagreement for very high multipoles and at lower redshifts.

Fig. 8 shows the correlation coefficient matrices at  $z_s = 0.6, 1.0, 2.0$  and  $3.0$  in a two-dimensional multipole space of  $(l, l')$ . The upper triangular parts of the matrices are the halo model prediction, while the lower triangular parts are the simulation results from our 1000 realizations. The correlations are generally stronger at higher  $l$  and at lower redshift, as expected.

#### 4.4. Signal-to-Noise Ratio

The obtained covariance matrices can be used to estimate the expected signal-to-noise ( $S/N$ ) ratio for measuring the lensing power spectrum. The cumulative signal-to-noise ratio can be defined (e.g. Takada & Jain 2004, 2009) as

$$\left(\frac{S}{N}\right)^2 = \sum_{l, l' \leq l_{\max}} P_\kappa(l) \text{Cov}^{-1}[P_\kappa(l), P_\kappa(l')] P_\kappa(l'), \quad (21)$$

where  $\text{Cov}^{-1}$  is the inverse of the covariance matrix and the power spectrum information over  $72 \lesssim l \leq l_{\max}$  is included ( $l = 72$  is the fundamental mode of our ray-tracing simulations,  $l_f \simeq 2\pi/5^\circ \simeq 72$ ). The signal-to-noise ratio is independent of the bin width, as long as the convergence power spectrum does not rapidly vary within bin width.

Fig. 9 shows the  $S/N$  for the convergence power spectrum as a function of maximum multipole  $l_{\max}$  for  $z_s = 0.6, 0.8, 1.0, 1.5, 2.0$  and  $3.0$ . The dotted line shows  $S/N$

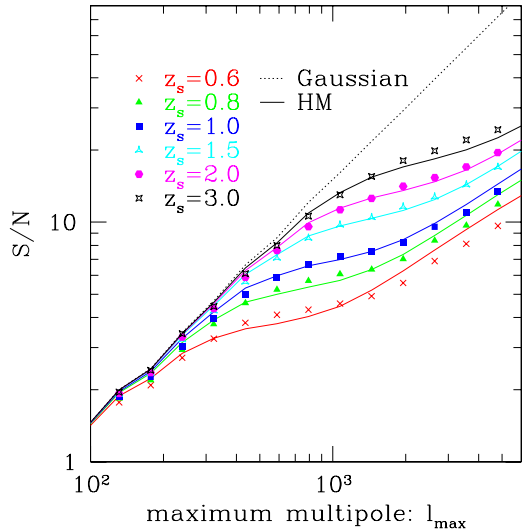


FIG. 9.— The cumulative signal-to-noise ratio ( $S/N$ ) for the convergence power spectrum is shown as a function of maximum multipole  $l_{\max}$  at  $z_s = 0.6, 0.8, 1.0, 1.5, 2.0$  and  $3.0$ , where the power spectrum information over a range of multipoles  $72 \leq l \leq l_{\max}$  is included. The solid curves show the halo model predictions, while the dotted line is the result for the Gaussian covariance case.

when only Gaussian errors are included. Our simulation results suggest that the  $S/N$  begins to deviate significantly from that of the Gaussian case. It increases slowly with increasing  $l_{\max}$  in the non-linear regime. The  $S/N$  for low redshift surveys does not increase significantly at multipoles from a few hundreds to 1000. This implies that there is little gain in the  $S/N$  even if including modes at the larger  $l$ , as has been found in the previous works (Rimes & Hamilton 2005; Hamilton et al. 2006; Neyrinck et al. 2006; Neyrinck & Szapudi 2007; Takahashi et al. 2009; Doré et al. 2009). The simulation results show that the  $S/N$  is degraded by non-Gaussian covariances by up to factor 5 for source redshift  $z_s = 1.0$ . Lee & Pen (2008) measured the Fisher information content for the angular power spectrum of SDSS galaxies, which is equivalent to the  $S/N$  defined in Eq. (21). They found a similarly significant saturation of the  $S/N$ .

The simulation results can be compared with the halo model predictions, where the non-Gaussian errors are computed from the halo model, and the power spectrum and the Gaussian term of covariance are taken from the simulation results in the  $S/N$  calculation. The halo model predictions are again in a good agreement with the simulation results, and in particular well capture complex dependences of the  $S/N$  on multipoles and source redshifts.

For planned weak lensing surveys most important range of multipoles are around  $l \sim 1000$  in order to avoid complications due to effects of strong nonlinear clustering and gas dynamics on mass power spectrum. Over such a range of multipoles the cosmological non-Gaussian errors are dominant over the shot noise due to intrinsic galaxy shapes, therefore the effect needs to be properly taken into account to obtain unbiased, secure extraction of cosmological parameters from the measured power spectrum (see Takada & Jain (2009) for the similar discussion).



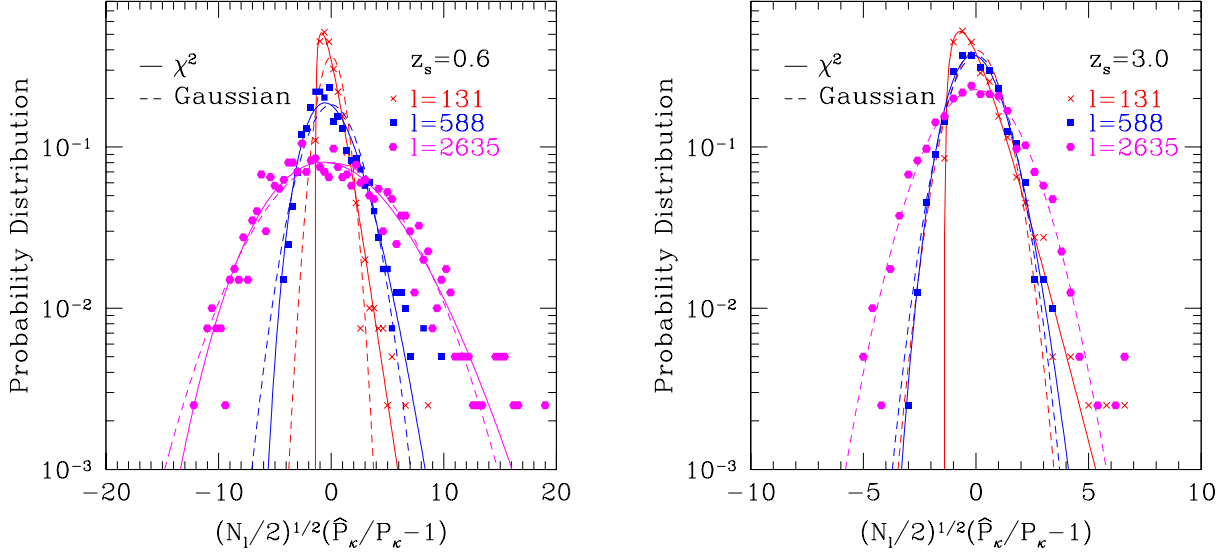


FIG. 10.— Probability distribution of the convergence power spectrum estimators  $\hat{P}_\kappa$  among the 1000 realizations for  $z_s = 0.6$  (left panel) and  $3.0$  (right), respectively. The solid and dashed curves show the  $\chi^2$ - and Gaussian-distributions with zero mean, respectively, where the variance is set to the to the diagonal covariance components measured from the simulations.

In this section, we study the probability distribution of the convergence power spectrum estimator  $\hat{P}_\kappa$  in order to see how the non-linear growth causes a non-Gaussian distribution in the convergence power spectrum estimators. It should be noted that the convergence power spectrum covariance simply reflects the width of the full distribution at each  $l$ .

Fig. 10 shows the probability distribution of the convergence power spectrum estimators  $\hat{P}_\kappa$  among 1000 realizations. We measure the probability distribution for  $(N_l/2)^{1/2}(\hat{P}_\kappa/P_\kappa - 1)$  so that the mean and variance of the distribution are equals to zero and unity in the linear regime or if the convergence field is Gaussian. The probability distribution is normalized so as to give unity when integrated over all  $\hat{P}_\kappa$  values. For large  $l$  values, the distribution is broadened due to non-linear evolution. The solid and dashed curves show the  $\chi^2$ -distribution and the expected Gaussian distribution, respectively, where the variance for each of the distributions is set to the diagonal term of covariance measured from simulations at each  $l$ , i.e. the variance includes the non-Gaussian covariance contribution as given in Fig. 6. To be more explicit, assuming that the estimate  $\hat{P}_\kappa$  obeys the  $\chi^2$ -distribution, the mean and variance are set to  $P_\kappa(l)$  and  $\text{Cov}[P_\kappa(l), P_\kappa(l)]$  (replacing  $\hat{P}(k) \rightarrow \hat{P}_\kappa(l)$ ,  $N_k/2 \rightarrow P_\kappa^2(l)/\text{Cov}[P_\kappa(l), P_\kappa(l)]$  in Eq. (B1) in Takahashi et al. (2009)). Fig. 10 shows that the probability distribution is well approximated by the  $\chi^2$ -distribution, but display a larger positive tail than expected from the  $\chi^2$ -distribution. One can see that the estimators have a skewed distribution, even for the low multipoles such as  $l \sim 100$  where the lensing fields are more in the linear regime.

The deviations from a Gaussian distribution can be quantified by studying skewness  $S_3$  and kurtosis  $S_4$  of

the distribution in Fig. 10:

$$S_3 = \frac{\langle (\hat{P}_\kappa(l) - P_\kappa(l))^3 \rangle}{\langle (\hat{P}_\kappa(l) - P_\kappa(l))^2 \rangle^{3/2}},$$

$$S_4 = \frac{\langle (\hat{P}_\kappa(l) - P_\kappa(l))^4 \rangle}{\langle (\hat{P}_\kappa(l) - P_\kappa(l))^2 \rangle^2} - 3. \quad (22)$$

If the convergence field is a Gaussian random field, which is a good approximation in linear regime, the convergence power spectrum estimator  $\hat{P}_\kappa$  of a given  $l$  exactly obeys the  $\chi^2$ -distribution. In this case, the skewness and kurtosis can be analytically computed as

$$S_3 = \sqrt{\frac{4 \text{Cov}[P_\kappa(l), P_\kappa(l)]}{P_\kappa(l)^2}}, \quad S_4 = \frac{6 \text{Cov}[P_\kappa(l), P_\kappa(l)]}{P_\kappa(l)^2}. \quad (23)$$

Note that  $S_3$  and  $S_4$  scale with survey area as  $S_3 \propto \Omega_s^{-1/2}$  and  $S_4 \propto \Omega_s^{-1}$ , as  $\text{Cov} \propto \Omega_s^{-1}$ .

Fig. 11 shows the simulation results for  $S_3$  and  $S_4$  as a function of multipole  $l$ . Note that the results in Fig. 11 are for a survey area of  $\Omega_s = 25$  degree<sup>2</sup>. The solid curves are the theoretical predictions of Eq. (23). The model well describes the simulation results for  $z_s = 3.0$ , while the results for  $z_s = 0.6$  show significant non-Gaussian cumulants over a range of multipoles we have considered, due to stronger non-linearities. For  $z_s = 3.0$ , both  $S_3$  and  $S_4$  asymptote to zero at high  $l$ , i.e. the probability distribution approaches to a Gaussian distribution at high  $l$  due to the central limit theorem.

Since the skewness and the kurtosis have non-negligible values at multipoles relevant for future surveys, a prior knowledge on the full distribution may be needed to obtain an unbiased estimate on the ensemble averaged band power at each  $l$  bin.

## 6. CONCLUSION AND DISCUSSION

Accurate statistics are essential in the likelihood analysis for future precision cosmology. We can exploit the

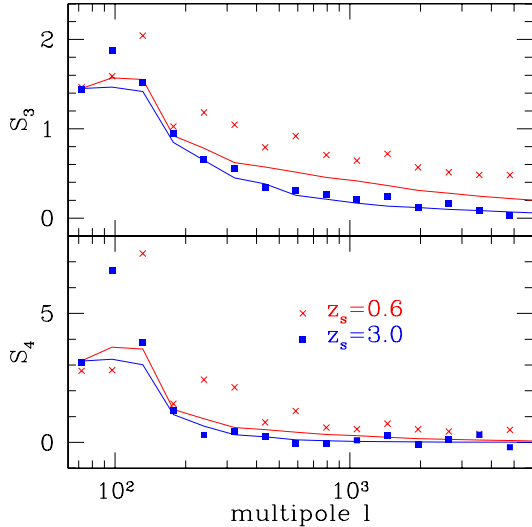


FIG. 11.— The skewness (top panel) and the kurtosis (bottom) of the convergence power spectrum distribution as a function of multipole  $l$  at  $z_s=0.6$  and  $3.0$ . The solid curves are the theoretical predictions from Eq. (23).

full potential of upcoming high quality data, only if we use appropriate statistical methods. For weak-lensing surveys, non-linear gravitational evolution of large-scale structure can significantly compromise cosmological parameter estimations and thus needs to be modelled accurately.

We have used ray-tracing simulations in order to study how the non-Gaussian covariance varies with scales and redshifts for the standard  $\Lambda$ CDM cosmology. We have performed a total of 1000 independent ray-tracing simulations using 400 cosmological  $N$ -body simulations. The non-Gaussian errors become more significant on smaller scales and at lower redshifts. The cumulative signal-to-noise ratio ( $S/N$ ) for measuring lensing power spectrum is degraded due to non-Gaussian covariance by up to a factor of 5 for a weak lensing survey to  $z_s \sim 1$ . We show that the simulation results are fairly well described by the halo model prediction including additional contribution due to the statistical fluctuations in the number of halos in a finite survey volume.

We also study the probability distribution of the convergence power spectrum estimator among 1000 realizations. The probability distribution has a large skewness especially for shallow surveys, which is likely due to non-linear gravitational evolution. Therefore, a prior knowledge on the full distribution may be needed to obtain an unbiased estimate on the ensemble averaged band power at each  $l$ . Overall, the non-Gaussian errors likely cause best-fitting parameters to be systematically biased, if the model fitting is done improperly assuming the Gaussian covariances. Therefore it is clearly needed to develop an appropriate method for parameter estimations from the measured power spectrum taking into account the non-Gaussian errors.

The most conventionally used statistical measure is the cosmic shear correlation function. An invaluable feature of the correlation function is that it does not require non-trivial corrections for survey geometry and masking effects. Therefore, it is useful to estimate the covariance matrix of real space correlation function and to derive fitting formula to calibrate the full covariances for an arbitrary survey area. These issues will be studied in a subsequent paper.

We would like to thank Issha Kayo for useful comments and discussions. We also thank the anonymous referee for careful reading of our manuscript and very useful suggestions. This work is supported in part by World Premier International Research Center Initiative (WPI Initiative), and by Grant-in-Aid for Scientific Research on Priority Areas No. 467 “Probing the Dark Energy through an Extremely Wide and Deep Survey with Subaru Telescope” and by the Grant-in-Aid for Nagoya University Global COE Program, “Quest for Fundamental Principles in the Universe: from Particles to the Solar System and the Cosmos”, from the Ministry of Education, Culture, Sports, Science and Technology of Japan. Numerical computations were in part carried out on the general-purpose PC farm at Center for Computational Astrophysics, CfCA, of National Astronomical Observatory of Japan.

## REFERENCES

- Bacon, D. J., Refregier, A. R., & Ellis, R. S. 2000, *MNRAS*, 318, 625
- Bartelmann, M., & Schneider, P. 2001, *Phys. Rep.*, 340, 291
- Cooray, A., & Hu, W. 2001, *ApJ*, 554, 56
- Cooray, A., & Sheth, R. 2002, *Phys. Rep.*, 372, 1
- Doré, O., Lu, T., & Pen, U.-L. 2009, arXiv:0905.0501
- Eifler, T., Schneider, P., & Hartlap, J. 2009, *A&A*, 502, 721
- Fosalba, P., Gaztañaga, E., Castander, F. J., & Manera, M. 2008, *MNRAS*, 391, 435
- Fu, L., et al. 2008, *A&A*, 479, 9
- Hamana, T., & Mellier, Y. 2001, *MNRAS*, 327, 169
- Hamana, T., et al. 2003, *ApJ*, 597, 98
- Hamilton, A. J. S., Rimes, C. D., & Scoccimarro, R. 2006, *MNRAS*, 371, 1188
- Heitmann, K., White, M., Wagner, C., Habib, S., & Higdon, D. 2008, arXiv:0812.1052
- Hilbert, S., Hartlap, J., White, S. D. M., & Schneider, P. 2009, *A&A*, 499, 31
- Hockney, R. W., & Eastwood, J. W. 1988, *Computer simulation using particles* (Bristol: Hilger, 1988)
- Hu, W. 1999, *ApJ*, 522, L21
- Hu, W., & Kravtsov, A. V. 2003, *ApJ*, 584, 702
- Huterer, D. 2002, *Phys. Rev. D*, 65, 063001
- Ichiki, K., Takada, M., & Takahashi, T. 2009, *Phys. Rev. D*, 79, 023520
- Jain, B., Seljak, U., & White, S. 2000, *ApJ*, 530, 547
- Jarvis, M., Jain, B., Bernstein, G., & Dolney, D. 2006, *ApJ*, 644, 71
- Kaiser, N. 1998, *ApJ*, 498, 26
- Kaiser, N., Wilson, G., & Luppino, G. A. 2000, arXiv:astro-ph/0003338
- Lee, J., & Pen, U.-L. 2008, *ApJ*, 686, L1
- Lewis, A., Challinor, A., & Lasenby, A. 2000, *ApJ*, 538, 473
- Limber, D. N. 1954, *ApJ*, 119, 655
- Ma, C.-P., & Fry, J. N. 2000, *ApJ*, 531, L87
- Miyazaki, S., et al. 2006, in Presented at the Society of Photo-Optical Instrumentation Engineers (SPIE) Conference, Vol. 6269, Society of Photo-Optical Instrumentation Engineers (SPIE) Conference Series
- Navarro, J. F., Frenk, C. S., & White, S. D. M. 1997, *ApJ*, 490, 493
- Neyrinck, M. C., & Szapudi, I. 2007, *MNRAS*, 375, L51

- Neyrinck, M. C., Szapudi, I., & Rimes, C. D. 2006, MNRAS, 370, L66
- Peacock, J. A., & Smith, R. E. 2000, MNRAS, 318, 1144
- Reid, B. A., & Spergel, D. N. 2009, ApJ, 698, 143
- Rimes, C. D., & Hamilton, A. J. S. 2005, MNRAS, 360, L82
- Scoccimarro, R., Zaldarriaga, M., & Hui, L. 1999, ApJ, 527, 1
- Seljak, U. 2000, MNRAS, 318, 203
- Semboloni, E., et al. 2006, A&A, 452, 51
- Semboloni, E., van Waerbeke, L., Heymans, C., Hamana, T., Colombi, S., White, M., & Mellier, Y. 2007, MNRAS, 375, L6
- Sheth, R. K., & Tormen, G. 1999, MNRAS, 308, 119
- Smith, R. E., et al. 2003, MNRAS, 341, 1311
- Spergel, D. N., et al. 2007, ApJS, 170, 377
- Springel, V. 2005, MNRAS, 364, 1105
- Springel, V., et al. 2005, Nature, 435, 629
- Takada, M., & Bridle, S. 2007, New Journal of Physics, 9, 446
- Takada, M., & Jain, B. 2003a, MNRAS, 340, 580
- Takada, M., & Jain, B. 2003b, MNRAS, 344, 857
- Takada, M., & Jain, B. 2004, MNRAS, 348, 897
- Takada, M., & Jain, B. 2009, MNRAS, 395, 2065
- Takahashi, R., et al. 2009, ApJ, 700, 479
- Teyssier, R., et al. 2009, A&A, 497, 335
- Vale, C., & White, M. 2003, ApJ, 592, 699
- Van Waerbeke, L., & Mellier, Y. 2003, arXiv:astro-ph/0305089
- Van Waerbeke, L., et al. 2000, A&A, 358, 30
- White, M., & Hu, W. 2000, ApJ, 537, 1
- White, M., & Vale, C. 2004, Astroparticle Physics, 22, 19
- Wittman, D. M., Tyson, J. A., Kirkman, D., Dell'Antonio, I., & Bernstein, G. 2000, Nature, 405, 143
- Zhang, P., & Sheth, R. K. 2007, ApJ, 671, 14